PHYSICAL REVIEW MATERIALS **3**, 074007 (2019)

Coexisting 1T/2H polymorphs, reentrant resistivity behavior, and charge distribution in MoS_2-hBN 2D/2D composite thin films

Swati Parmar,[1,2] Abhijit Biswas,[1] Sachin Kumar Singh,[1] Bishakha Ray,[3] Saurabh Parmar,[3] Suresh Gosavi,[4]
Vasant Sathe,[5] Ram Janay Choudhary,[5] Suwarna Datar,[3,*] and Satishchandra Ogale[1,†]
[1]*Department of Physics and Centre for Energy Science, Indian Institute of Science Education and Research Pune, Maharashtra 411008, India*
[2]*Department of Technology, Savitribai Phule Pune University, Maharashtra 411007, India*
[3]*Defense Institute of Advanced Technology, Pune, Maharashtra 411025, India*
[4]*Department of Physics, Savitribai Phule Pune University, Maharashtra 411007, India*
[5]*UGC-DAE Consortium for Scientific Research, Indore 452001, India*

(Received 13 April 2019; revised manuscript received 31 May 2019; published 25 July 2019)

In view of their immensely intriguing properties, two-dimensional (2D) materials are being intensely researched in search of novel phenomena and diverse application interests; however, studies on the realization of 2D/2D nanocomposites in the application-worthy thin-film platform are rare. Here we have grown MoS_2-hexagonal boron nitride (hBN) 2D/2D composite thin films on different substrates by the pulsed laser deposition technique and made comparative studies with the pristine MoS_2 and hBN films. The Raman and x-ray photoelectron spectroscopy techniques as well as high-resolution transmission electron microscopy confirm the concomitant presence of both the 1T (conducting) and 2H (semiconducting) polymorphs of MoS_2 in the composite film. Interestingly, a peculiar reentrant semiconductor-metal-insulator transition is seen in the MoS_2-hBN 2D/2D composite film which is absent in the MoS_2 film, and it correlates well with the signatures of phonon softening seen in temperature-dependent Raman spectroscopy. Furthermore, electrostatic force microscopy reveals the presence of three distinct regions (metallic, semiconducting, and insulating) in the MoS_2-hBN composite film with differing contact potentials and enhanced propensity for charge transfer with respect to pristine MoS_2. A triboelectric nanogenerator device containing biphasic MoS_2-hBN composite film as an electron acceptor exhibits more than twofold (sixfold) enhancement in peak-to-peak output voltage as compared to the pristine MoS_2 (hBN) film. These observations bring out the potential of 2D/2D nanocomposite thin films for unfolding emergent phenomena and technological applications.

DOI: 10.1103/PhysRevMaterials.3.074007

I. INTRODUCTION

Since the discovery of graphene, there has been a significant growth of interest and activity in the field of two-dimensional (2D) materials in view of their unique set of physical properties driven by surface effects as well as quantum size effects which render a special nature to their electronic density of states [1–4].

Among the list of numerous 2D materials of past and emergent interest, MoS_2 is the second most explored material after graphene and has been studied in various applications for over a decade [5]. As an *n*-type transition-metal dichalcogenide semiconductor, MoS_2 exhibits astonishingly diverse, tunable, and application-worthy physical, chemical, mechanical, and optical properties [6–13]. These include superconductivity [10], metal-insulator transition [11], and topological insulator [12] properties. One of the remarkable features of MoS_2 is that it shows multiple polymorphs, the primary polymorphs being 1T (trigonal phase), 1H and 2H (hexagonal phase), and 3R (rhombohedral phase). Among these, the 1T polymorph, which is a paramagnetic metal [14], is thermodynamically the least stable one and tends to form the stable 2H phase by reorganizing its stacking layers. Ubiquitously, coexistence of two or more structural phases can influence the material functionalities in interesting ways [15–18]. However, stabilizing the multiphase state (e.g., 1T and 2H phases of MoS_2) is challenging due to the differing stabilizing conditions for different phases. Various synthetic methods, e.g., chemical exfoliation, hydrothermal method, and chemical vapour deposition, have been examined to achieve the multiphase states [17,18]. Importantly, it has been shown that MoS_2 exhibits phase change from semiconductor (2H) to metal (1T) and enhanced hydrogen evolution reaction (HER) activity due to significantly higher electrical conductivity, useful for device fabrications [19,20].

Although several interesting works have been reported in the literature on the growth of large area thin films of 2D materials and their heterostructures [7], attempts at the growth of multiphase stabilized 2D/2D nanocomposites in the device application-worthy *thin-film* form of contemporary device interest are rare [21]. There is thus a quest for a new route to realize this objective. It is also of great interest to explore the application potential of the films which could be more in the form of mosaics of nanoscale sheets (turbostratic configuration), rather than a single- or few-layer large area uniform coatings. Such a configuration renders a

---

[*] suwarnadatar@diat.ac.in

[†] satishogale@iiserpune.ac.in

natural benefit of retaining and expressing the properties of *few-layer forms* of these 2D materials in a thin-film assembly. In this context, the pulsed laser deposition (PLD) technique allows a great flexibility of stoichiometry, layer thickness, and growth temperature or ambient control, enabling growth of different thin-film configurations, their heterostructures, or even superlattices. Keeping this in mind, we have chosen hexagonal boron nitride (hBN), another prominent layered 2D material to grow nanocomposite films of MoS_2 and hBN, with a hope to induce and stabilize the multiphase in MoS_2 (1T and 2H phases in the present paper, which henceforth we will call *biphasic*), because of the specific PLD growth dynamics as well as strong interlayer coupling between MoS_2 and hBN [22]. hBN is also intensely researched material due to its exotic optoelectronic properties, mechanical robustness, and thermal stability. It has been extensively studied for various device applications, e.g., field effect transistors, detectors, and photoelectric devices [22,23]. It is an insulator with a large band gap of ~6 eV, an atomically flat surface without any dangling bonds, charge impurities, and, importantly, it is chemically inert [24–26].

In this paper, relying on the specific strengths and advantages of the PLD technique, we have successfully stabilized biphasic 2D material by growing thin films of the 2D/2D MoS_2-hBN system using a single composite target. Biphasic nature was confirmed by Raman and x-ray photoelectron spectroscopy. Temperature-dependent Raman spectra show the signature of phonon mode softening with decreasing temperature. Interestingly, in our MoS_2-hBN composite case, the temperature-dependent resistivity shows an intriguing reentrant semiconductor-metal-insulator transition as a consequence of competing polymorphs, which is absent in MoS_2 film. Electrostatic force microscopy (EFM) reveals the presence of three distinct regions (metallic, semiconducting, and insulating) in the composite films with the observation of three different contact potentials, respectively. In addition, EFM study without and with charge injection on the surface reveals the electron acceptor character of the composite case with enhanced propensity for charge transfer vis-à-vis the pristine MoS_2. Furthermore, a triboelectric nanogenerator (TENG) device containing biphasic MoS_2-hBN thin film as an electron acceptor shows more than twofold (sixfold) increase in the output voltage with respect to the pristine MoS_2 (hBN) thin films.

II. THIN-FILM GROWTH

For this paper, we have grown ~200-nm pristine MoS_2, hBN, and composite MoS_2-hBN thin films on c-Al_2O_3 (0001) and n-Si substrates by PLD (KrF laser, wavelength 248 nm). A schematic of a typical PLD growth is shown in Fig. 1. A polycrystalline target of MoS_2-hBN was made by using the solid-state reaction method. For this, MoS_2 and hBN powders were mixed (1:1 molar ratio) and sintered in argon atmosphere for 8 h at 750 °C. MoS_2 and hBN targets were also made by following the conventional solid-state reaction methods. Prior to the deposition, the substrates were annealed at 1000 °C for 1 h to make them atomically flat as confirmed by atomic force microscopy, revealing clear step features (see Supplemental Material Fig. S1 [27]). The target to substrate distance was kept at ~40 mm. All the films were grown at a substrate temperature of 500 °C at a pulse repetition rate of 10 Hz using a laser energy density of 0.5 J/cm^2, in the presence of 5-mTorr argon pressure. Additionally, we have grown films on flexible Kapton substrates (grown at 400 °C while keeping the other growth conditions the same) for device fabrications.

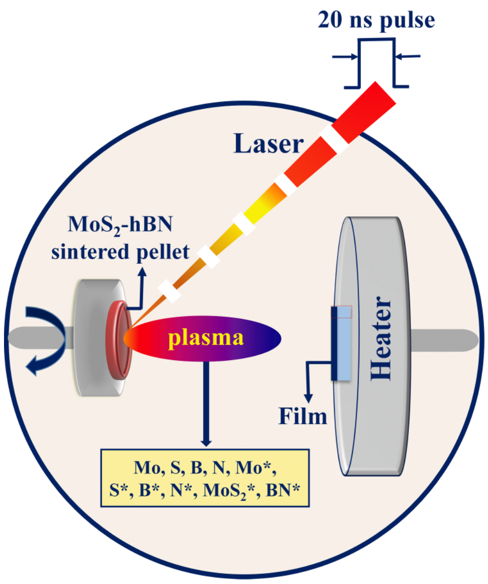

FIG. 1. Schematic of the pulsed laser deposition setup for growing MoS_2, hBN, and MoS_2-hBN thin films. Plasma generated after laser ablation of target consists of high-energy (0.1–10 eV) ions and radicals of Mo, S, B, and N.

In the PLD process depicted in Fig. 1, it should be noted that the pulses of 5-eV photons dump a significant amount of energy (density) in the 20-ns time scale onto the substrate surface, causing highly nonequilibrium phenomena leading to the formation of a plasma plume wherein various ionic and radical species are present. They progress towards the hot substrate with a fairly high velocity distribution. On the substrate surface, the impinging radicals seek equilibrium or near-equilibrium phase formation based on the temperature and simultaneously impinging atoms/ions of the ambient temperature. The semiequilibrium solubility and miscibility criteria of the potentially developing phases then govern the final phase fractions and their character in the film. As discussed and evidenced through detailed characterizations later, this process leads to a state wherein N doped MoS_2 sheets coexist with hBN sheets in the form of a mosaic or turbostratic assembly. It is interesting to note that although Mo, S, B, and N related ions and radicals impinge on the surface during PLD the growth equilibria render the two chemically distinct separate phases.

III. RESULTS AND DISCUSSION

A. Raman spectroscopy

First, the Raman spectra of MoS_2-hBN thin films were recorded with a 2.33-eV (532 nm) excitation energy laser (Fig. 2). The main E_{1g}, E_{2g}, and A_{1g} peaks were observed at 285.4, 381.9, and 408 cm^{-1}, which correspond to the vibration of atoms along in-plane (E_{1g}, E_{2g}) and out-of-plane (A_{1g})

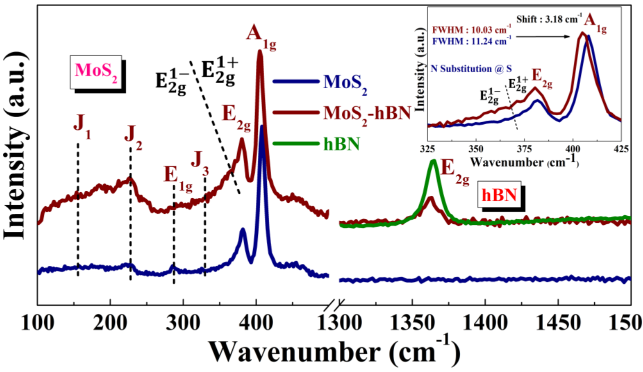

FIG. 2. Raman spectra of MoS_2, hBN, and MoS_2-hBN composite thin films grown on c-Al_2O_3 substrate, showing the presence of both 1T and 2H phases of MoS_2. The left side of the x-axis break is for MoS_2 signatures (100 to 500 cm^{-1}) and the right side of the break is for hBN (1300 to 1500 cm^{-1}).

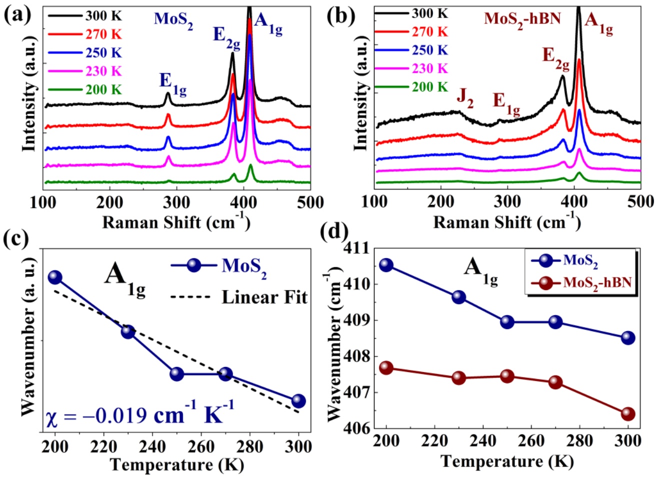

FIG. 3. (a), (b) Temperature-dependent Raman spectra of MoS_2 and MoS_2-hBN thin films, respectively, within the temperature range of $200 \leqslant T \leqslant 300$ K. (c) Temperature dependence of the A_{1g} phonon mode of MoS_2. (d) Comparison between temperature dependence of the A_{1g} phonon mode of MoS_2 and biphasic MoS_2-hBN composite film.

directions, respectively. It is clearly seen that the E_{2g} peak is redshifted by $\sim 1.5\,cm^{-1}$ as compared to the pristine case and splits into two peaks, labeled as ${E_{2g}}^{1+}$ and ${E_{2g}}^{1-}$. This peak splitting is attributed to the symmetry breaking of the E_{2g} vibrational mode as a consequence of the introduction of lattice strain due to *in situ* N doping and interface formation with hBN [28]. We also observed a significant amount of redshift ($\sim 4\,cm^{-1}$) in the A_{1g} mode. The shifts in the A_{1g} and E_{2g} modes in biphasic MoS_2-hBN thin film with respect to the pristine MoS_2 reflect the sensitivity of these modes to strain and doping in MoS_2 [29,30]. The shifts and broadening also indicate strong interlayer coupling between MoS_2 and hBN. More importantly, the observed significant enhancement of the J_1, J_2, and J_3 phonon modes at lower wave numbers in the composite film (see Fig. 2 and Supplemental Material Fig. S2 [27]) as compared to the pristine MoS_2 case implies a significant 1T component in the composite case [31]. We also observed that the characteristic peak of the E_{2g} phonon mode at $\sim 1365\,cm^{-1}$ in the pristine hBN case is redshifted by $\sim 2\,cm^{-1}$ in the composite case and appears significantly weaker and broader, implying the random strain generated during the growth [32].

The Raman spectroscopy data for the MoS_2 and MoS_2-hBN at selected temperatures ($200 \leqslant T \leqslant 300$ K) are shown in Figs. 3(a) and 3(b). These data are later discussed in the context of the interesting reentrant resistivity transition. The modes were fitted using the Lorentzian function, and the position of the A_{1g} mode thus obtained is plotted as a function of temperature in Fig. 3(c). The mode position of the MoS_2 shows a linear behavior apart from small but noticeable deviation around $T = 250$ K. The temperature coefficient of the frequency of this mode obtained by applying a linear fit to the data points results in the rate coefficient (χ) as $-0.019\,cm^{-1}\,K^{-1}$. This value is close to the one reported for MoS_2 [33]. In Fig. 3(d), the wave numbers corresponding to the A_{1g} mode of the MoS_2 and MoS_2-hBN layers are plotted as a function of temperature. It is seen that the modes show a redshift with increasing temperature for the MoS_2 layer, as reported before. Such a behavior is attributed to the anharmonic contributions to the interatomic potential energy, mediated by phonon-phonon interactions. On the other hand, the position of the A_{1g} mode for the MoS_2-hBN layer shows a very subtle reduction when temperature is increased. Interestingly, the mode position shows a significant reduction above $T = 240$ K. The first-principles density functional theory calculations on MoS_2 have clearly established that electron-phonon coupling is stronger in the case of the A_{1g} mode than that of the E_{2g} mode [30]. In another *ab initio* study of the interatomic force constants, separating the short-range and the long-range Coulomb parts, it is shown that the dielectric screening decreases the frequency of optical phonon modes [34]. Hence, it can be expected that an increase in dielectric constant and dielectric screening would occur, as the system contains insulating hBN layers. This increased dielectric screening is thus causing the decrease in frequency of the Raman mode below $T = 240$ K. Thus, our temperature-dependent Raman spectroscopy studies clearly show a modulation in phonon frequency of the A_{1g} mode. Following Chakraborty *et al.* [30], the A_{1g} mode is highly sensitive to the electron-phonon interaction, which is naturally going to affect the electronic transport due to softening of the mode frequency.

B. X-ray photoelectron spectroscopy

The x-ray photoelectron spectroscopy (XPS) data for the individual cases of the MoS_2 and hBN films along with those for the composite film are shown in Fig. 4(a). Specifically, the Mo $3p$ characteristic in MoS_2 films solely represents the presence of the 2H phase. The XPS data of Fig. 4(b) for the composite film (dark red) show broader distribution of the primary Mo $3p_{3/2}$ contributions with some structure. In the same figure we have shown the directly (arithmetically) added (MoS_2 + hBN) contributions from Fig. 4(a), to reveal departure from the simply mixed spectral states due to the composite formation. It is clear that the departure emanates primarily from the development of complex Mo-N coordination reflecting doping of N in MoS_2 [28]. Another possibility

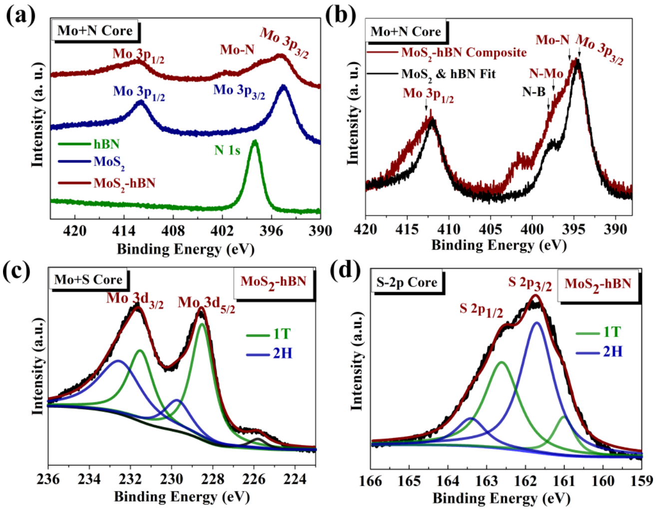

FIG. 4. XPS spectra of MoS_2, hBN, and MoS_2-hBN composite thin films grown on c-Al_2O_3 substrates. (a) N 1s and Mo 3p cores of MoS_2, hBN, and MoS_2-hBN composite films (b) N 1s and Mo 3p cores of arithmetically added (MoS_2 + hBN) contribution compared with the MoS_2-hBN composite case. (c) Mo+S 3d core of MoS_2-hBN. (d) S 2p core for MoS_2-hBN.

of the presence of Mo (IV) via MoS_3 coordination cannot be ruled out.

In the Mo 3d region of the data for the composite case, the contributions again appear somewhat broader and can be fitted by multiple peaks as shown in Fig. 4(c). Interestingly, the two intense peaks at 229.6 eV (Mo $3d_{5/2}$) and 232.6 eV (Mo $3d_{3/2}$) correspond to the 2H phase of MoS_2 with the Mo^{4+} state [17,24], while the two other peaks (at 228.5 and 231.5 eV), relatively shifted to lower binding energies by ~1 eV, reflect the existence of the 1T phase [35,36]. This unambiguously confirms the coexistence of 2H (semiconducting) and 1T (metallic) phases in the composite sample. From the area coverage of the peaks, the phase proportion can be estimated to be 58% (1T): 42% 2H phase. In comparison, the Mo 3d region of the data for the pristine MoS_2 case clearly depicts the 2H phase of MoS_2 film (see Supplemental Material Fig. S3 [27]).

The S 2p core data for the composite case are presented in Fig. 4(d). Two broad doublets are seen in the spectrum which can be fitted by four peaks. The two doublets with the binding energies of 161.7 and 163.4 eV reveal the presence of the 2H phase of MoS_2 while the other two peaks at 160.8 and 162.6 eV reflect the presence of the metallic 1T phase. Thus, the biphasic nature of the composite is further confirmed from the S 2p spectral analysis.

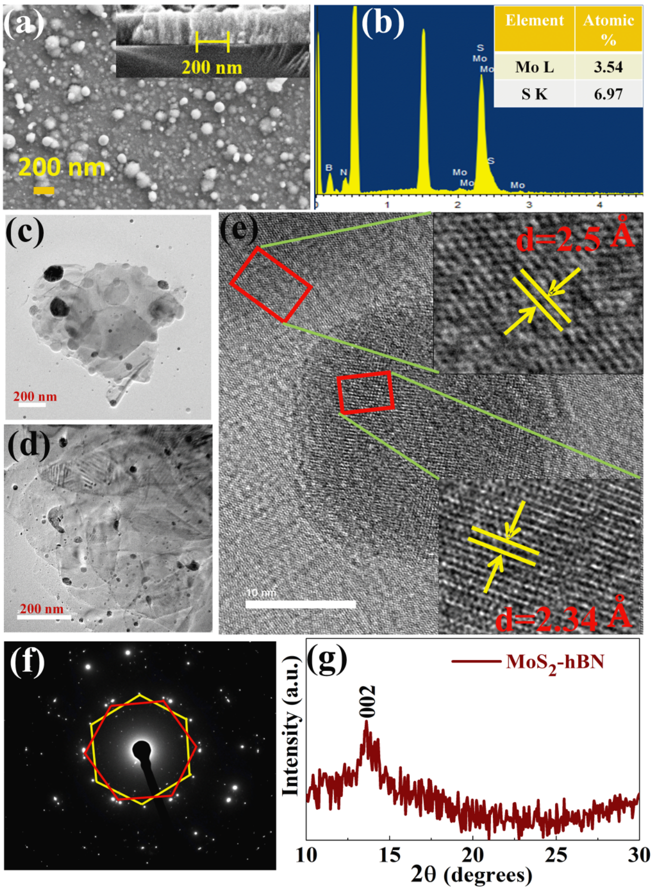

FIG. 5. (a) Top and side view (inset) FESEM images of MoS_2-hBN film grown on c-Al_2O_3. Typical grain size is ~50 nm (inset). (b) EDAX analysis of MoS_2-hBN grown on c-Al_2O_3 film confirms a 2:1 compositional ratio of Mo and S in the film; as is well known the lighter (low-Z) element (B, N) stoichiometry is not truthfully revealed by EDAX. (c)–(e) HRTEM images of MoS_2-hBN deposited on a carbon coated TEM grid at room temperature; the d spacing was found to be 2.34 Å (for MoS_2) and 2.5 Å (for hBN). (f) Selected area electron diffraction patterns with 30° angle-rotated spots confirm the concurrent presence of 1T and 2H phases of MoS_2. (g) X-ray diffraction shows the oriented nature of MoS_2-hBN grown on c-Al_2O_3 film.

C. High-resolution transmission electron microscopy, field-emission scanning electron microscopy, and x-ray diffraction

To elucidate the microscopic constitution of the films, we employed field-emission scanning electron microscopy (FESEM) with energy dispersive analysis of X-rays (EDAX) and high-resolution transmission electron microscopy (HRTEM) measurements. Figure 5(a) along with its inset present the FESEM data (top and side views) for the MoS_2-hBN film grown on sapphire substrate (typical grain size 50 nm), while the corresponding data for MoS_2 are shown in Supplemental Material Fig. S4 [27]. These data establish that the films are quite dense in all the cases, although the surfaces are noted to exhibit overgrowthlike features in the case of MoS_2-hBN composite film and flaky features in the case of only MoS_2 film. Due to significant charging during microscopy measurements, clean images could not be obtained in the case of h-BN films. Compositional analysis though EDAX is shown in Fig. 5(b). Technically, through EDAX, it is difficult to obtain the reliable compositional ratio of B and N as these are low-Z elements.

In view of the nonavailability of cross-section TEM imaging capability, for recording HRTEM data an interesting deposition strategy was adopted wherein a carbon coated holy grid was directly used as a substrate and an ultrathin film of the composite was grown thereupon. The HRTEM images of Figs. 5(c) and 5(d) clearly show that ultrathin sheetlike features are seen to have assembled during the PLD growth, which confirms the mosaic or turbostratic arrangement. The lattice image and its analysis shown in Fig. 5(e) further show that the film is indeed in the form of a 2D/2D heterostructure of MoS_2 and h-BN. Confirmation of the coexistence of the 1T and 2H phases in the sample was also obtained from the HRTEM analyses. Indeed, the biphasic nature of MoS_2 could be clearly revealed by the selected area electron diffraction pattern [Fig. 5(f)], with the spots identified with the red line representing the 2H-MoS_2 and the spots identified with the yellow line representing the 1T phase. The 2H phase has trigonal prismatic arrangement of Mo and S with AbA and BaB stacking, whereas the 1T phase has octahedral arrangement with AbC and AbC stacking. Therefore, in the 1T case the diffraction spots are usually angularly shifted from their ideal place in the basal plane by 30° (yellow line) [37]. As stated by Reshmi *et al.* [38], the *d* spacing of 2.34 Å [Fig. 5(e)] closely corresponds to (2 0 1) and (1 0 3) lattice constants of the 1T and 2H phase(s) of MoS_2, albeit with a degree of strain. The HRTEM of pristine cases MoS_2 and hBN shown in Supplemental Material Fig. S5 [27] also shows the corresponding *d* value of 2.2 and 2.5 Å, respectively.

As stated above, the HRTEM images of Figs. 5(c) and 5(d) show that the growth appears to be in the form of a dense mosaic of ultrathin MoS_2 and hBN sheets. This implies that the orientation of the film should be reflected to be along the *c* axis in the XRD pattern. This is indeed the case, as shown in Fig. 5(g) and for the pristine MoS_2 case (see Supplemental Material Fig. S6 [27]) [39].

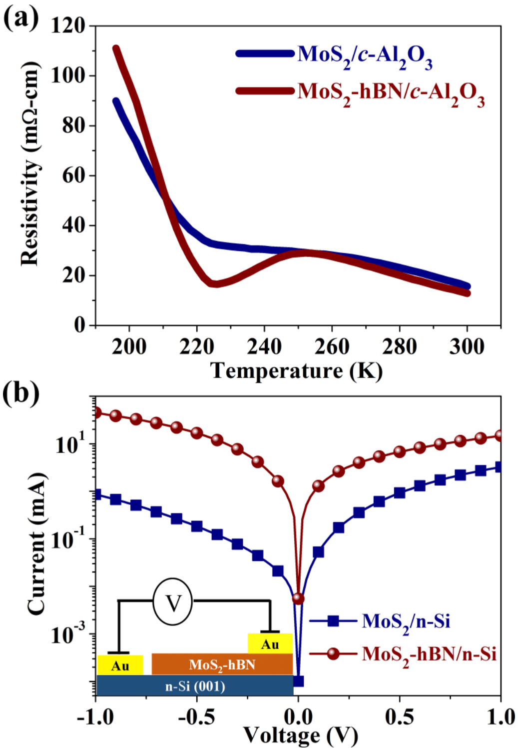

FIG. 6. (a) Resistivity of MoS_2 and biphasic MoS_2-hBN composite thin films grown on *c*-Al_2O_3 substrate. (b) Current perpendicular to plane transport of MoS_2 and MoS_2-hBN thin films grown on *n*-type Si (001) substrate. The hBN films are highly resistive, hence the corresponding data are not shown.

D. Electronic transport properties

Electronic transport in 2D material is known to be very sensitive to external perturbations (e.g., pressure, strain, and liquid gating) [6–9]. For example, 2H phase MoS_2 shows a semiconductor to metal transition as a consequence of reduction in S-S interlayer distance, induced by the applied high external pressure of ∼19 GPa [40]. Since our composite film consists of both the semiconducting (2H) and metallic (1T) phases as well as doping of nitrogen at the sulphur site (as seen from XPS and Raman data), it is highly interesting to investigate the electrical transport of the composite film.

Indeed, the result of the temperature-dependent in-plane four probe resistivity measurement of the biphasic MoS_2-hBN thin film [Fig. 6(a)] shows a highly peculiar semiconductor-metal-insulator reentrant transition in resistivity. This can certainly be attributed to the presence of a metallic 1T phase that gets stabilized in the composite case alone, while the MoS_2 itself leads only to the semiconducting 2H phase and shows the semiconductor-insulator transition while lowering the temperature. While cooling the biphasic film from $T = 300$ K, it shows a semiconducting behavior, while within the temperature range of $225 \leqslant T \leqslant 250$ K a drop is observed in resistivity, a clear signature of a semiconductor-to-metal transition. Below $T \leqslant 225$ K, again it makes a transition to the insulating state. A similar feature in the electronic transport was also observed by applying very high external pressure up to ∼35 GPa [41]. In the metallic region, the resistivity follows linear temperature dependence ($\rho \propto T$) [see Supplemental Material Fig. S7(a) [27]] as generally found in a normal metal. The insulating region was fitted with the three-dimensional variable range-hopping model ($\ln\rho \propto T^{-1/4}$) [see Supplemental Material Fig. S7(b) [27]] associated with the presence of disorder. The activation energy (E_A) was found to be ∼0.145 eV. Similar behavior was also observed in pristine MoS_2 under very high pressure as a consequence of competing phases as well as occurrence of charge density waves [42].

We also examined the current-perpendicular-to-plane (CPP) transport in the MoS_2 and MoS_2-hBN films in view of the intrinsic anisotropic nature of the films. The CPP transport was measured across MoS_2/n-Si and MoS_2-hBN/n-Si interfaces by sweeping voltage from −1 to 1 V at a scan rate of 62 mV/s. In the CPP transport, the top contact for the I-V measurements was gold (Au). The corresponding data with *n*-Si bottom and Au contact on the top are shown in Fig. 6(b), with the convention that the voltage is considered positive (on the *x* axis) when a positive potential is applied to the top of the composite film. It is immediately noted that the current at a given voltage is significantly (over an order of magnitude) higher under reverse bias and also substantially higher under forward bias. This might be attributed to the fact that the conductivity contribution emanating from the metallic 1T phase present in the biphasic sample is not laterally connected to enable percolation, but in the vertical configuration it could either connect/percolate or contribute via tunneling through ultrathin hBN sheets in the layered mosaic composite films. The bias asymmetry of the curves is seen to be reversed between the MoS_2 and MoS_2-hBN composite cases. Given the same contacts on the two sides in both the cases, this feature suggests a change in the nature of majority carriers. Interestingly, the resistivity difference is not noted to be as significant in the case of four probe in-plane resistivity shown in Fig. 6(a). This asymmetry between the in-plane and CPP transport signifies the presence of a specific constitution of the conducting 1T phase component.

E. Electrostatic force microscopy

Since a composite film composed of mixed semiconducting and metallic polymorphs of MoS_2 and insulating hBN layers has multiple interesting interfaces, these can have interesting consequences for the charge distributions in the layer and the corresponding response to external applied field. To confirm the distribution and field response of the electronic charges over the surface, we performed the electrostatic force microscopy analysis. EFM was performed in two-pass liftoff mode. The first pass was for atomic force microscopy morphology study and the second pass for EFM was at the height of 50 nm. Qualitatively the topography image shows surface roughness of the sample and the EFM phase image shows the electrical nature of the sample in different regions. Different phases present in the EFM data depict surface potential or work function difference between various components in the sample. The topography and the corresponding EFM phase image of the composite sample at a bias voltage of 3 V were also obtained [see Supplemental Material Figs. S8(a) and S8(b) [27]]. One can identify at least three different phase contrasts (A, B, and C) in the image marked by circles; this is also confirmed from the histogram, showing three maxima [see Supplemental Material Fig. S8(c) [27]].

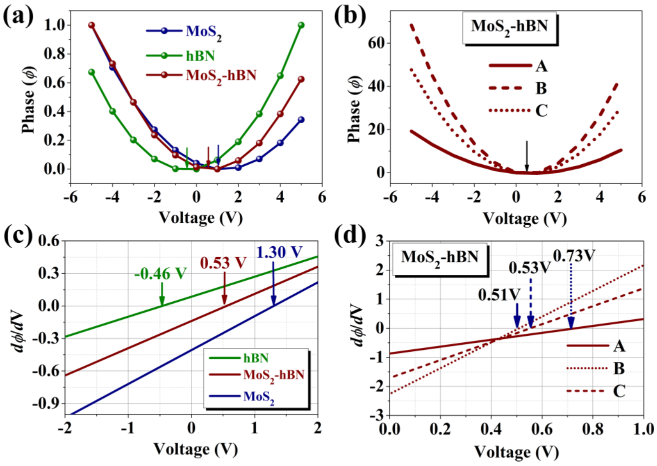

FIG. 7. (a) Electrostatic force microscopy of phase vs voltage spectra calculated from EFM images of the surface of MoS_2, hBN, and biphasic MoS_2-hBN film grown on *c*-Al_2O_3 for the applied voltages (−5 to +5 V), depicting the clear difference in work function compared to pristine cases. (b) EFM phase shift of MoS_2-hBN for the applied voltages (−5 to +5 V) shows the asymmetric nature as well as the minor difference in the work function indicative of the charge distribution in the film at different areas. The solid parabolic curve is the least-square fit to the data. (c), (d) Contact potential difference in three different films and in three different regions of the composite MoS_2-hBN film.

Quantitatively the EFM phase shift is directly related to the local surface potential described as

$$\Delta\phi = -\arcsin\left[\frac{Q}{2k}\frac{d^2C}{dz^2}(V_{\text{tip}} - V_{\text{surface}})^2\right],$$

where $\Delta\phi$ is the phase shift, Q is the quality factor and k is the force constant of the cantilever, $\frac{d^2C}{dz^2}$ is the second derivative of the capacitance between the sample and the probe as a function of the vertical distance, V_{tip} is the dc bias applied to the tip, and V_{surface} is the local surface potential on the sample surface [43]. To estimate the local surface potential variation in hBN, MoS_2, and MoS_2- hBN, a plot of phase shifts at different biases between the film and the tip, measured by EFM phase, with a fixed lift height of 50 nm was obtained and fitted with the least-square measurement to the above-mentioned equation as shown in Figs. 7(a) and 7(b). All the curves are parabolic, which confirms the proportional interaction variation with $(V_{\text{tip}} - V_{\text{surface}})^2$, which is indicative of contact potential difference (CPD) between the tip and the surface. The surface potential can be attributed to charge distribution in real space or work function difference between the tip and the sample depending on whether the sample is insulating, semiconducting, or conducting. Several factors can contribute to the local charge distribution in the case of insulators, like humidity, tip-sample interaction, adsorption of charged ions, etc. As indicated in Fig. 7(c), hBN films have a surface potential of −0.46 eV, which could be because of adsorbed charges from the ambient condition. Therefore, to better understand the nature of the charges, the surface potential of hBN is plotted with respect to the applied bias voltage to the tip, which clearly shows that change in the surface potential after negative polarization is much greater than that of the positive polarization, indicative of the presence of trapped sites for negative charges present in the sample. Further, as shown in the same figure, the contact potential difference for MoS_2 is 1.3 V. Assuming the tip work function to be 5.6 eV for the platinum tip, the work function of MoS_2 films can be estimated to be 4.3 eV, which matches with the reported work function for MoS_2 in ambient conditions. Further, CPD for the composite was observed to be lowered as shown in Fig. 7(c). To investigate this further, data were taken at various sites on the composite, which indicated different phases in the image. The fitted data for the composite as shown in the figure show that the work function of the MoS_2 seems to have increased, showing at least two distinct work function values of 4.87 and 5.09 eV [Figs. 7(c) and 7(d)]. This indicates that two different phases of MoS_2 have indeed been formed, as also observed by other techniques.

To further investigate the effect of hBN in biphasic MoS_2-hBN film on the formation of constituents with different work functions in the film, charges were injected in the film using a conducting tip, following a procedure discussed by Zhao *et al.* [44]. This was done by taking the tip towards the sample in contact mode with an applied bias voltage of ±10 V and then later imaging the area for smaller applied bias voltage. It was observed that there was no change in the EFM image after injecting charges by applying +10 V,

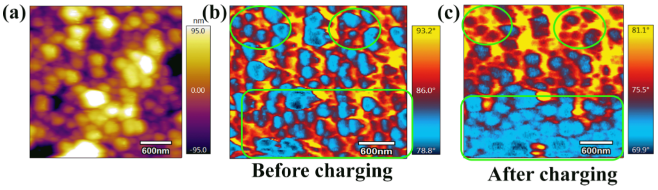

FIG. 8. EFM images of MoS_2-hBN film at tip bias 4 V: (a) topography image, (b) EFM phase image before charging, and (c) EFM phase image after charging at −10 V.

whereas one can clearly see that charges have been injected in the film for −10 V, clearly indicating that there are trapped sites for negative charges which have been introduced after the formation of the composite (Fig. 8). The topographic image and corresponding line profile, before and after charging, are shown in Supplemental Material Fig. S9 [27]. However, no influence of the charge injection was found on pristine MoS_2 film (see Supplemental Material Fig. S10 [27]). Therefore, hBN and related interfaces seem to have provided sites for trapped charges by means of formation of interfaces of different work functions which are related to the changes in CPD, affecting the electron transfer process. As extensively discussed by Seol *et al.* [20], such distributions can have interesting consequences for triboelectric nanogenerator applications of 2D materials. Hence, we proceeded to examine this aspect in a preliminary study, as discussed below.

F. Triboelectric nanogenerator

Triboelectric nanogenerator devices based on 2D materials are becoming a cutting-edge research area for future mechanical energy harvesting. Therefore, based on the EFM data discussed above, we explored our biphasic MoS_2-hBN thin films as an electron acceptor in a TENG configuration in comparison with the pristine MoS_2 case [20]. We designed a TENG device as shown in Fig. 9(a). For this we grew biphasic MoS_2-hBN (and also MoS_2 and hBN) films on a flexible Kapton substrate at 400 °C, by keeping all the other growth conditions the same in PLD. The lower growth temperature for Kapton substrate as compared to the 500 °C used for sapphire or silicon substrate was based on the consideration of the thermal stability of Kapton. The morphology of the film was found to be slightly rougher as compared to that on the sapphire and silicon substrates, however the Raman spectrum (see Supplemental Material Fig. S11 [27]) showed that the basic character of the film was essentially of biphasic nature. The small difference noted was the lower tailing of the E_{2g} peak, suggested to be due to nitrogen doping of MoS_2. Interestingly the other signatures of the 1T phase (namely, J_1, J_2, and J_3) are quite well defined in this case.

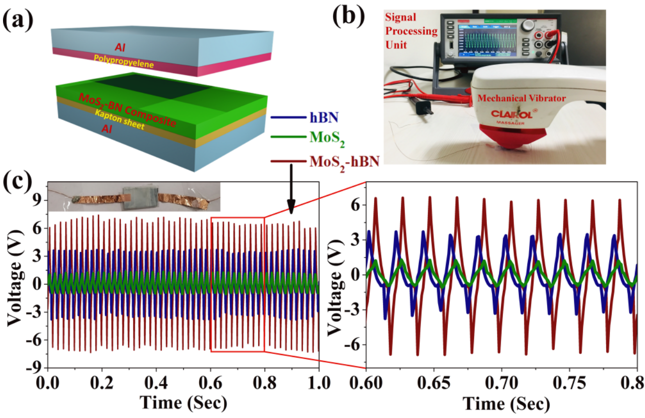

FIG. 9. (a) Schematic of the device architecture of TENG made of composite biphasic MoS_2-hBN composite thin films. (b) TENG performance measurement setup. (c) The continuous output voltage signal of TENG devices (MoS_2, hBN, and MoS_2-hBN) recorded at 50-Hz frequency.

The MoS_2-hBN on Kapton and a polypropylene sheet on top of it were sandwiched between two aluminum layers; copper wires were soldered to the electrodes from the top and bottom sides. The area of the sample was 5 × 10 mm. The mechanical input was applied by a vibrator at 50 Hz with a measured force of 10 N [Fig. 9(b)]. The output open circuit voltage (no load resistance) values obtained for hBN, MoS_2, and MoS_2-hBN are shown in Fig. 9(c), while the same is shown on the expanded scale for clarity about the shape of the signals. It can be clearly seen that the open circuit voltages for hBN, MoS_2, and MoS_2-hBN have a ratio of 6: 3: 1. Thus, there is a twofold increase of average peak-to-peak output voltage for the MoS_2-hBN (∼14.7 V) case vis-à-vis pristine MoS_2 (∼7.2 V). In contrast, composite film shows sixfold increase in average peak-to-peak output voltage with respect to pristine hBN (∼2.3 V). This is consistent with the propensity of biphasic film for charging effects under field as reflected by the EFM data. We also estimated the powering capability of the devices based on the three cases by adding a load of 1 MΩ (see Supplemental Material Fig. S12 [27]). Here again the composite case shows a higher power delivery. A comparison table in terms of overall TENG performance based on 2D materials is as given in Supplemental Material Table S1 [27]. Finally, but interestingly, the shape of the TENG voltage signal curves is peculiar and has been noted before only in the case of 2D materials [45]. We will undertake further studies to optimize and enhance the TENG performance in subsequent studies.

IV. CONCLUSIONS

Summarizing, we have used the pulsed laser deposition technique to stabilize the metastable metallic 1T phase in significant proportion (>50%) along with the highly stable 2H phase of MoS_2 in supported thin film grown on single-crystalline substrates. Our detailed chemical and microstructural characterizations by XPS, Raman spectroscopy, and HRTEM confirm the presence of the biphasic nature of the composite films. Temperature-dependent Raman spectra show the signature of phonon mode softening and bear interesting correlation with the transport property, exhibiting a peculiar reentrant semiconductor-metal-insulator transition in the temperature-dependent resistivity only in the case of composite film. Electrostatic force microscopy without and with charge injection reveals the presence of three distinct regions (metallic, semiconducting, and insulating) in the composite film with differing contact potentials and electron acceptor character. A triboelectric nanogenerator device containing biphasic MoS_2-hBN composite film as an electron acceptor exhibits more than twofold (sixfold) enhanced peak-to-peak output voltage as compared to the pristine MoS_2 (hBN). This paper will pave the way to engineer new multiphasic 2D heterostructures via thin-film growth to obtain novel multifunctionalities.

ACKNOWLEDGMENTS

S.P. would like to thank CSIR for a SRF fellowship. S.O. would like to thank the DST Nanomission Thematic unit for funding support and the Department of Atomic Energy for the award of a Raja Ramanna fellowship and grant. A.B. would like to thank the government of India for providing SERB-N-PDF Fellowship No. PDF/2017/000313. We would like to thank Prof. Surjeet Singh and Ms. Prachi Telang for the temperature-dependent resistivity measurement. We would also like to thank Mr. Sharad Varma for the XPS measurements and Mr. Anil Shetty for the FESEM measurement.

---

[1] K. S. Novoselov, A. K. Geim, S. V. Morozov, D. Jiang, Y. Zhang, S. V. Dubonos, I. V. Grigorieva, and A. A. Firsov, Electric field effect in atomically thin carbon films, Science **306**, 666 (2004).

[2] A. C. Ferrari, F. Bonaccorso, V. Fal'ko, K. S. Novoselov, S. Roche, P. Bøggild, S. Borini, F. H. L. Koppens, V. Palermo, N. Pugno *et al.*, Science and technology roadmap for graphene, related two-dimensional crystals, and hybrid systems, Nanoscale **7**, 4598 (2015).

[3] W. Han, Perspectives for spintronics in 2D materials, APL Mater. **4**, 032401 (2016).

[4] Y. Liu, N. O. Weiss, X. Duan, H. C. Cheng, Y. Huang, and X. Duan, Van der Waals heterostructures and devices, Nat. Rev. Mater. **1**, 16042 (2016).

[5] H. S. S. Ramakrishna Matte, A. Gomathi, A. K. Manna, D. J. Late, R. Datta, S. K. Pati, and C. N. R. Rao, MoS_2 and WS_2 analogues of graphene, Angew Chemie. **49**, 4059 (2010).

[6] X. Duan, C. Wang, A. Pan, R. Yu, and X. Duan, Two-dimensional transition metal dichalcogenides as atomically thin semiconductors: Opportunities and challenges, Chem. Soc. Rev. **44**, 8859 (2015).

[7] Z. Lin, A. McCreary, N. Briggs, S. Subramanian, K. Zhang, Y. Sun, X. Li, N. J. Borys, H. Yuan, S. K. Fullerton-Shirey, A. Chernikov, H. Zhao, S. McDonnell, A. M. Lindenberg, K. Xiao, B. J. LeRoy, M. Drndić, J. C. M. Hwang, J. Park, M. Chhowalla, R. E. Schaak, A. Javey, M. C. Hersam, J. Robinson, and M. Terrones, 2D materials advances: from large scale synthesis and controlled heterostructures to improved characterization techniques, defects and applications, 2D Mater. **3**, 042001 (2016).

[8] S. Manzeli, D. Ovchinnikov, D. Pasquier, O. V. Yazyev, and A. Kis, 2D transition metal dichalcogenides, Nat. Rev. Mater. **2**, 17033 (2017).

[9] Q. H. Wang, K. Kalantar-Zadeh, A. Kis, J. N. Coleman, and M. S. Strano, Electronics and optoelectronics of two-dimensional transition metal dichalcogenides, Nat. Nanotechnol. **7**, 699 (2012).

[10] J. T. Ye, Y. J. Zhang, R. Akashi, M. S. Bahramy, R. Arita, and Y. Iwasa, Superconducting dome in a gate-tuned band insulator, Science **338**, 1193 (2012).

[11] X. Chen, Z. Wu, S. Xu, L. Wang, R. Huang, Y. Han, W. Ye, W. Xiong, T. Han, G. Long, Y. Wang, Y. He, Y. Cai, P. Sheng, and N. Wang, Probing the electron states and metal-insulator transition mechanisms in molybdenum disulphide vertical heterostructures, Nat. Commun. **6**, 6088 (2015).

[12] X. Qian, J. Liu, L. Fu, and J. Li, Quantum spin Hall effect in two-dimensional transition metal dichalcogenides, Science **346**, 1344 (2014).

[13] Z. Lin, B. R. Carvalho, E. Kahn, R. Lv, R. Rao, H.Terrones, M. A. Pimenta, and M. Terrones, Defect engineering of two-dimensional transition metal dichalcogenides, 2D Mater. **3**, 022002 (2016).

[14] R. Kappera, D. Voiry, S. E. Yalcin, W. Jen, M. Acerce, S. Torrel, B. Branch, S. Lei, W. Chen, S. Najmaei, J. Lou, P. M. Ajayan, G. Gupta, A. D. Mohite, and M. Chhowalla, Metallic 1T phase source/drain electrodes for field effect transistors from chemical vapor deposited, APL Mater. **2**, 092516 (2014).

[15] K. Chang, X. Hai, H. Pang, H. Zhang, L. Shi, G. Liu, H. Liu, G. Zhao, M. Li, and J. Ye, Targeted synthesis of 2H- and 1T-phase MoS_2 monolayers for catalytic hydrogen evolution, Adv. Mater. **28**, 10033 (2016).

[16] B. Xia, P. Liu, Y. Liu, D. Gao, D. Xue, and J. Ding, Re doping induced 2H-1T phase transformation and ferromagnetism in MoS_2 nanosheets, Appl. Phys. Lett. **113**, 013101 (2018).

[17] H. Huang, Y. Cui, Q. Li, C. Dun, W. Zhou, W. Huang, L. Chen, C. A. Hewitt, and D. A. Carroll, Metallic 1T phase MoS_2 nanosheets for high-performance thermoelectric energy harvesting, Nano Energy **26**, 172 (2016).

[18] S. Shi, Z. Sun, and Y. H. Hu, Synthesis, stabilization and applications of 2-dimensional 1T metallic MoS_2 engineering of a multiphasic 1T/2H MoS_2, J. Mater. Chem. A **6**, 23932 (2018).

[19] Z. Hu, S. Zhang, Y. Zhang, D. Wang, H. Zeng, and L. Liu, Modulating the phase transition between metallic and semiconducting single-layer MoS_2 and WS_2 through size effects, Phys. Chem. Chem. Phys. **17**, 1099 (2015).

[20] M. Seol, S. Kim, Y. Cho, K. Byun, H. Kim, J. Kim, S. K. Kim, S. W. Kim, H. Shin, and S. Park, Triboelectric series of 2D layered materials, Adv. Mater. **30**, 1801210 (2018).

[21] A. Barvat, N. Prakash, D. K. Singh, A. Dogra, S. P. Khanna, S. Singh, and P. Pal, Mixed phase compositions of MoS_2 ultra thin film grown by pulsed laser deposition, Mater. Today. Proc. **5**, 2241 (2018).

[22] S. Wang, X. Wang, and J. H. Warner, All chemical vapor deposition growth of MoS_2:h-BN vertical van der Waals heterostructures, ACS Nano **9**, 5246 (2015).

[23] K. Zhang, Y. Feng, F. Wang, Z. Yang, and J. Wang, Two dimensional hexagonal boron nitride (2D-hBN): Synthesis, properties and applications, J. Mater. Chem. C **5**, 11992 (2017).

[24] K. N. Duerloo, M. T. Ong, and E. J. Reed, Intrinsic piezoelectricity in two-dimensional materials, J. Phys. Chem. Lett. **3**, 2871 (2012).

[25] J. Qi, X. Qian, L. Qi, J. Feng, D. Shi, and J. Li, Strain-engineering of band gaps in piezoelectric boron nitride nanoribbons, Nano Lett. **12**, 1224 (2012).

[26] K. H. Michel and B. Verberck, Phonon dispersions and piezoelectricity in bulk and multilayers of hexagonal boron nitride, Phys. Rev. B **83**, 115328 (2011).

[27] See Supplemental Material at http://link.aps.org/supplemental/10.1103/PhysRevMaterials.3.074007 for morphological, crystallinity, electronic properties, and electrostatic force microscopy analysis.

[28] A. Azcatl, X. Qin, A. Prakash, C. Zhang, L. Cheng, Q. Wang, N. Lu, M. J. Kim, J. Kim, K. Cho, R. Addou, C. L. Hinkle, J. Appenzeller, and R. M. Wallace, Covalent nitrogen doping and compressive strain in MoS_2 by remote N_2 plasma exposure, Nano Lett. **16**, 5437 (2016).

[29] C. Rice, R. J. Young, R. Zan, and U. Bangert, Raman-scattering measurements and first-principles calculations of strain-induced phonon shifts in monolayer, Phys. Rev. B **87**, 081307(R) (2013).

[30] B. Chakraborty, A. Bera, D. V. S. Muthu, S. Bhowmick, U. V. Waghmare, and A. K. Sood, Symmetry-dependent phonon renormalization in monolayer MoS_2 transistor, Phys. Rev. B **85**, 161403(R) (2012).

[31] D. Voiry, A. Mohite, and M. Chhowalla, Phase engineering of transition metal dichalcogenides, Chem. Soc. Rev. **44**, 2702 (2015).

[32] R. V. Gorbachev, I. Riaz, R. R. Nair, R. Jalil, L. Britnell, B. D. Belle, E. W. Hill, K. S. Novoselov, K. Watanabe, T. Taniguchi, A. K. Geim, and P. Blake, Hunting for monolayer boron nitride: Optical and Raman signatures, Small **7**, 465 (2011).

[33] A. M. Thripuranthaka, R. V. Kashid, C. S. Rout, and D. J. Late, Temperature dependent Raman spectroscopy of chemically derived few layer MoS_2 and WS_2 nanosheets, Appl Phys. Lett. **104**, 081911 (2014).

[34] A. Molina-Sánchez and L. Wirtz, Phonons in single-layer and few-layer MoS_2 and WS_2, Phys. Rev. B **84**, 155413 (2011).

[35] X. Geng, W. Sun, W. Wu, B. Chen, A. Al-Hilo, M. Benamara, H. Zhu, F. Watanabe, J. Cui, and T. P. Chen, Pure and stable metallic phase molybdenum disulfide nanosheets for hydrogen evolution reaction, Nat. Commun. **7**, 10672 (2016).

[36] M. Acerce, D. Voiry, and M. Chhowalla, Metallic 1T phase MoS_2 nanosheets as supercapacitor electrode materials, Nat. Nanotechnol. **10**, 313 (2015).

[37] M. K. Jana and C. N. R. Rao, Two-dimensional inorganic analogues of graphene: Transition metal dichalcogenides subject areas, Phil. Trans. R. Soc. A **374**, 2076 (2016).

[38] S. Reshmi, M. V. Akshaya, B. Satpati, P. K. Basu, and K. Bhattacharjee, Structural stability of coplanar 1T-2H superlattice MoS_2 under high energy electron beam, Nanotechnology **29**, 205604 (2018).

[39] S. N. Heo, Y. Ishiguro, R. Hayakawa, T. Chikyow, and Y. Wakayama, Perspective: Highly ordered MoS_2 thin films grown by multi-step chemical vapor deposition process, APL Mater. **4**, 030901 (2016).

[40] A. P. Nayak, S. Bhattacharyya, J. Zhu, J. Liu, X. Wu, T. Pandey, C. Jin, A. K. Singh, D. Akinwande, and J. F. Lin, Pressure-induced semiconducting to metallic transition in multilayered molybdenum disulphide, Nat. Commun. **5**, 3731 (2014).

[41] Z.-H. Chi, X.-M. Zhao, H. Zhang, A. F. Goncharov, S. S. Lobanov, T. Kagayama, M. Sakata, and X.-J. Chen, Pressure-Induced Metallization of Molybdenum Disulfide, Phys. Rev. Lett. **113**, 036802 (2014).

[42] Z. Y. Cao, J. W. Hu, A. F. Goncharov, and X. J. Chen, Nontrivial metallic state of MoS_2, Phys. Rev. B **97**, 214519 (2018).

[43] C. H. Lei, A. Das, M. Elliott, and J. E. Macdonald., Quantitative electrostatic force microscopy-phase measurements, Nanotechnology **15**, 627 (2004).

[44] P. Zhao, N. Soin, K. Prashanthi, J. Chen, S. Dong, E. Zhou, Z. Zhu, A. A. Narasimulu, C. D. Montemagno, L. Yu, and J. Luo, Emulsion electrospinning of polytetra fluoroethylene (PTFE) nano fibrous membranes for high-performance triboelectric nanogenerators, ACS Appl. Mater. Interfaces **10**, 5880 (2018).

[45] J. Lee, J. Y. Park, E. B. Cho, T. Y. Kim, S. A. Han, T. Kim, Y. Liu, S. K. Kim, C. J. Roh, H. Yoon, H. Ryu, W. Seung, J. S. Lee, J. Lee, and S. Kim, Reliable piezoelectricity in bilayer WSe_2 for piezoelectric nanogenerators, Avd. Mater. **29**, 1606667 (2017).